Best Practice & Research Clinical Endocrinology & Metabolism xxx (xxxx) xxx

Contents lists available at ScienceDirect

Best Practice & Research Clinical Endocrinology & Metabolism

journal homepage: www.elsevier.com/locate/beem

MAML3-fusions modulate vascular and immune tumour microenvironment and confer high metastatic risk in pheochromocytoma and paraganglioma

María Monteagudo[a,b,1], Bruna Calsina[c,1], Milton E. Salazar-Hidalgo[a], Ángel M. Martínez-Montes[a], Elena Piñeiro-Yáñez[d], Eduardo Caleiras[e], Maria Carmen Martín[f], Sandra Rodríguez-Perales[f], Rocío Letón[a], Eduardo Gil[c], Alexandre Buffet[g,h], Nelly Burnichon[g,h], Ángel Fernández-Sanromán[a], Alberto Díaz-Talavera[a,ad], Sara Mellid[a], Ester Arroba[a], Clara Reglero[a], Natalia Martínez-Puente[a,b], Giovanna Roncador[i], Maria Isabel del Olmo[j], Pedro José Pinés Corrales[k], Cristina Lamas Oliveira[k], Cristina Álvarez-Escolá[l], María Calatayud Gutiérrez[m], Adrià López-Fernández[n], Nuria Palacios García[o], Rita María Regojo[p], Luis Robles Díaz[q], Nuria Romero Laorden[r], Oscar Sanz Guadarrama[s], Nicole Bechmann[t], Felix Beuschlein[v,w,x], Letizia Canu[y], Graeme Eisenhofer[u], Martin Fassnacht[z,aa], Svenja Nölting[w], Marcus Quinkler[ab], Elena Rapizzi[y], Hanna Remde[aa], Henri J. Timmers[ac], Judith Favier[g,h], Anne-Paule Gimenez-Roqueplo[g,h], Cristina Rodriguez-Antona[a], Maria Currás-Freixes[c], Fatima Al-Shahrour[d], Alberto Cascón[a,ad], Luis J. Leandro-García[a], Cristina Montero-Conde[a,ad], Mercedes Robledo[a,ad,*]

[a] *Hereditary Endocrine Cancer Group; Human Cancer Genetics Program Spanish National Cancer Research Centre (CNIO), Madrid, Spain*

* Corresponding author at: Hereditary Endocrine Cancer Group; Human Cancer Genetics Program Spanish National Cancer Research Centre (CNIO), Madrid, Spain.

E-mail address: mrobledo@cnio.es (M. Robledo).

https://doi.org/10.1016/j.beem.2024.101931

Please cite this article as: M. Monteagudo, B. Calsina, M.E. Salazar-Hidalgo et al., *MAML3*-fusions modulate vascular and immune tumour microenvironment and confer high metastatic risk in pheochromocytoma and paraganglioma, Best Practice & Research Clinical Endocrinology & Metabolism, https://doi.org/10.1016/j.beem.2024.101931

[b] PhD Program in Neuroscience, Universidad Autonoma de Madrid-Cajal Institute, Madrid, Spain
[c] Familial Cancer Clinical Unit, Human Cancer Genetics Program Spanish National Cancer Research Centre (CNIO), Madrid, Spain
[d] Bioinformatics Unit, Structural Biology Program, Spanish National Cancer Research Centre (CNIO), Madrid, Spain
[e] Histopathology Core Unit Biotechnology Program Spanish National Cancer Research Centre (CNIO), Madrid, Spain
[f] Molecular Citogenetic Unit Human Cancer Genetics Program Spanish National Cancer Research Centre (CNIO), Madrid, Spain
[g] Département de médecine génomique des tumeurs et des cancers, AP-HP, Hôpital Européen Georges Pompidou, Paris, France
[h] Université Paris Cité, Inserm, PARCC, Paris, France
[i] Monoclonal Antibodies Core Unit Biotechnology Program Spanish National Cancer Research Centre (CNIO), Madrid, Spain
[j] Department of Endocrinology and Nutrition, University Hospital La Fe, Valencia, Spain
[k] Department of Endocrinology and Nutrition Albacete University Hospital, SESCAM, Albacete, Spain
[l] Department of Endocrinology, La Paz University Hospital, Madrid, Spain
[m] Department of Endocrinology and Nutrition 12 de Octubre University Hospital, Madrid, Spain
[n] Department of Medical Oncology, Vall d'Hebrón Hospital, Barcelona, Spain
[o] Department of Endocrinology, Puerta de Hierro University Hospital, Madrid, Spain
[p] Department of Pathology, La Paz University Hospital, Madrid, Spain
[q] Department of Oncology, 12 de Octubre University Hospital, Madrid, Spain
[r] Department of Medical Oncology, La Princesa University Hospital, Madrid, Spain
[s] Department of General Surgery, University Hospital of León, León, Spain
[t] Institute for Clinical Chemistry and Laboratory Medicine Faculty of Medicine and University Hospital Carl Gustav Carus Technische Universität Dresden, Dresden Germany, Germany
[u] Department of Medicine III University Hospital Carl Gustav Carus Technische Universität Dresden, Dresden, Germany
[v] Medizinische Klinik und Poliklinik IV Klinikum der Universität München, Munich, Germany
[w] Klinik für Endokrinologie Diabetologie und Klinische Ernährung UniversitätsSpital Zürich, Zürich, Switzerland
[x] LOOP Zurich - Medical Research Center, Zurich, Switzerland
[y] Department of Experimental and Clinical Medicine University of Florence, Florence, Italy
[z] Department of Internal Medicine I Division of Endocrinology and Diabetes University Hospital Würzburg University of Würzburg, Würzburg, Germany
[aa] Comprehensive Cancer Center Mainfranken University of Würzburg, Würzburg, Germany
[ab] Endocrinology in Charlottenburg Stuttgarter Platz 1, Berlin, Germany
[ac] Department of Internal Medicine, Radboud University Medical Centre, Nijmegen, the Netherlands
[ad] Centro de Investigación Biomédica en Red de Enfermedades Raras (CIBERER), Madrid, Spain

ARTICLE INFO

Article history:
Available online xxxx

Keywords:
MAML3-fusion
metastasis
pheochromocytoma
paraganglioma
MAML3 screening procedure
tumour microenvironment
vasculature

Pheochromocytomas and paragangliomas are rare neuroendocrine tumours. Around 20–25 % of patients develop metastases, for which there is an urgent need of prognostic markers and therapeutic stratification strategies. The presence of a *MAML3*-fusion is associated with increased metastatic risk, but neither the processes underlying disease progression, nor targetable vulnerabilities have been addressed. We have compiled a cohort of 850 patients, which has shown a 3.65 % fusion prevalence and represents the largest *MAML3*-positive series reported to date. While *MAML3*-fusions mainly cause single pheochromocytomas, we also observed somatic post-zygotic events, resulting in multiple tumours in the same patient. *MAML3*-tumours show increased expression of neuroendocrine-to-mesenchymal transition markers, MYC-targets, and angiogenesis-related genes, leading to a distinct tumour microenvironment with unique vascular and immune profiles. Importantly, our findings have identified *MAML3*-tumours specific vulnerabilities beyond Wnt-pathway dysregulation, such as a rich vascular network, and

[1] These authors equally contributed to this study.

overexpression of PD-L1 and CD40, suggesting potential therapeutic targets.

Introduction

Pheochromocytomas (PCCs) and paragangliomas (PGLs), collectively known as PPGLs, are rare neuroendocrine tumours derived from the chromaffin cells of the adrenal medulla and paraganglia, respectively. These tumours are genetically heterogeneous and are associated with germline and somatic pathogenic variants (PV) in more than 20 genes described so far [1,2]. PPGLs display distinct expression profiles determined by specific driver genes, leading to their classification into three clusters: pseudohypoxic (C1), kinase signalling (C2), and Wnt-altered (C3). The latter cluster comprises tumours with *MAML3*-fusions and *CSDE1*-PV [3]. Metastatic disease occurs in approximately 20 % of the PPGL patients, with an overall 5-year survival rate of 40–77 % [4], and current treatments show limited efficacy. Tumour size (≥ 5 cm), extra-adrenal location, and *SDHB*-PV are key prognostic factors [4–6], though clinical outcomes remain mostly unpredictable [6–8]. Therefore, accurate molecular markers for metastatic risk and personalized treatment strategies are needed to improve patient management.

Genomic studies have elucidated the molecular landscape of PPGLs [3,9]. Our recent large-scale genomic study on metastatic PPGLs provided crucial insights into this aggressive tumour subset [10]. Notably, this study identified a classifier using four molecular events – high microsatellite instability (MSI) score, high *CDK1* expression, *ATRX*-PV and *MAML3*-fusions – that achieved 100 % sensitivity in predicting metastatic risk at the time of primary tumour diagnosis [10].

MAML3-fusion related PPGLs show a distinct transcriptional and methylation profile and are associated with an aggressive tumour behaviour [3]. MAML3 regulates the transcription of NOTCH pathway genes by binding to the NOTCH intracellular domain (NICD). By contrast, MAML3-fusion proteins with UBTF or TCF4 as fusion partners, lack this binding motive and its canonical function [11] is altered by activating the Wnt signalling pathway and increasing β-catenin protein levels [3,11].

Despite the rarity of *MAML3*-driven tumours, understanding their metastatic behaviour and identifying drug vulnerabilities is essential. Here, we gathered publicly available and novel transcription and methylation data to explore their specific characteristics. Our findings indicate a 3.65 % prevalence of the fusion and a significant association with a shorter time to progression, along with a tendency to accumulate additional alterations in bona fide progression genes such as *TERT* and *ATRX*. Moreover, these tumours show increased expression of neuroendocrine-to-mesenchymal transition (Ne-MT) markers, MYC-targets, and angiogenesis-related genes. Consequently, we conducted a comprehensive study of the *MAML3*-tumour microenvironment (TME), revealing distinct vascular architecture and immune infiltration patterns with therapeutic implications.

Materials and methods

Series and clinical data

The 779-patient cohort analysed in this study incorporates transcriptomic and methylation data from our group (CNIO series 1 and 2, and CNIO microarrays) and 3 published accessible cohorts (Supplementary Table 1). Transcriptional data from CNIO series 1 comprises 114 samples from 105 patients with PPGL (previously reported series [10]). CNIO series 2 includes 81 additional samples from 74 PPGL patients with available clinical information (Table 1) on tumour behaviour, sex, age at first tumour diagnosis and presence of single or multiple PPGLs. Tumours were classified as aggressive if they exhibited capsular or adipose tissue invasion, vascular infiltration, or showed multiple recurrences without definitive evidence of metastatic disease. PD-L1 immunohistochemistry (IHC) and break-apart fluorescence in situ hybridization (FISH) studies included samples from 84 patients (Supplementary Table 2).

Table 1
Clinical characteristics of 74 new patients in the CNIO series 2.

Patient´s clinical characteristics	New CNIO patients (n = 74)
Primary tumor localization	
PCC	57 % (42)
PGL	25 % (19)
Multiple PGL	3 % (2)
PCC+PGL	7 % (5)
Metastasis	5 % (4)
NA	3 % (2)
Sex	
Female	49 % (36)
Male	47 % (35)
NA	4 % (3)
Age at initial diagnosis of PCC/PGL; median (range) in years	48 (14–80)
Clinical behavior	
Non-metastatic disease	67 % (50)
Aggressive disease	7 % (5)
Metastatic disease	26 % (19)

Only patients who had provided informed consent were included in the study, in compliance with the principles of the Declaration of Helsinki. The protocol was approved by the following Ethics Committees: Hospital Universitario 12 de Octubre (15/024), Madrid, Spain; Universitäts Spital Zurich (2017–00771), Zurich, Switzerland; Klinikum der Universität (379–10), Munich, Germany; University of Würzburg (88/11), Würzburg, Germany; Azienda Ospedaliera Universitaria Careggi (Prot. N. 2011/0020149), Florence, Italy; Berlin Chamber of Physicians (Eth-S-R/14), Berlin, Germany; Radboud University Medical Center (9803–0060), Nijmegen, The Netherlands; University Hospital Carl Gustav Carus at TU Dresden (EK210052017 and EK189062010), Dresden, Germany.

Molecular characterization of PPGL series: driver pathogenic variants and secondary events involving ATRX and TERT

The 81 new tumour samples were collected either in formalin-fixed paraffin-embedded (FFPE) or fresh-frozen (FF) and tumour selection (> 80% cancer cells) was performed by a pathologist (E.C.) on haematoxylin and eosin-stained slides. DNA and RNA isolation, quality control and library preparation were performed as previously described [10]. The prepared libraries were subsequently sequenced on a NovaSeq™ system (Illumina).

Germline and somatic PV in PPGL driver genes were characterized using NGS AmpliSeq Custom DNA Panel (Illumina, San Diego, CA, USA), and confirmed by Sanger sequencing. *TERT* promoter (C228T and C250T mutations) and *ATRX*-PV were analysed in all CNIO tumour samples using a customized NGS panel [12]. While *ATRX*-PV data were available from The Cancer Genome Atlas (TCGA) and COMETE-derived series [3,13], *TERT* promoter mutational status was only described in the latter [13]. However, to acquire complete information on *TERT* status, *TERT* expression, *TERT* promoter hypermethylation and/or copy number gains were analysed in the whole series [12–15].

MAML3-fusion candidates identification

MAML3-fusion candidates were identified through different approaches: (1) using a gene expression signature (n = 765) and a methylation probe one (n = 568), (2) FISH, and (3) PD-L1 IHC in samples with available FFPE material. Study workflow is summarized in Supplementary Figure 1.

Identification of MAML3-fusion candidates using a gene expression signature

ComBat-seq was used to merge the new CNIO series 2 (n = 81) with the CNIO series 1 + TCGA dataset generated by Calsina et al., 2023, and publicly available data sets (COMETE-derived [16], Evenepoel [14] and CNIO microarrays [17]) (Supplementary Figure 1). These six series were combined by Z-score,

selecting the genes described in the TCGA transcriptomic profile as associated with *MAML3*-fusion (*DVL3*, *MYC*, *WNT4*, *NKD1*, *FZD7*, *WNT5B*, *WNT7B*, *MAML3*, *PTCH1*, *GLI2*, *FZD3*, *FZD8* and miR-375) [3]. MicroRNA (miRNA) data was extracted from Calsina et al., 2019 [18] and merged into the same matrix by applying the same z-score transformation. Through hierarchical clustering based on Euclidian distance, tumours clustering together with previously reported *MAML3*-cases [3,10,13] were categorized as *MAML3*-fusion candidates.

Identification of MAML3-fusion candidates using a hypomethylated probes signature

First, we identified approximately 3000 differentially methylated probes between *MAML3*-fusion cases and other genotypes (log fold change [logFC] > 1 and False Discovery Rate [FDR] < 0.05) using Illumina Infinium HumanMethylation450 BeadChip data in the TCGA series [3] genotypes. Among these probes, 243 were also present on the Illumina Infinium HumanMethylation27 BeadChip, which was the platform used by most of the methylation data available (Supplementary Table 1). To merge the data from these 243 probes across three methylation cohorts (CNIO [19–22], TCGA [3] and COMETE-derived [9]) into a single matrix, beta-values of these probes were z-score transformed. By hierarchical clustering using Jaccard distance, tumours clustering together with previously reported *MAML3*-cases [3,10,13] were categorized as *MAML3*-fusion candidates.

Break-apart FISH assay for MAML3-fusion identification

A dual-colour break-apart FISH probe was developed using six bacterial artificial chromosome (BAC) clones from BACPAC Genomics (Supplementary Figure 2a).

Three BAC clones (RP11–6A22, RP11–615B12, and RP11–903H21) located in *MAML3* 5′ region were labelled with Spectrum-Green using the Nick translation assay (Sigma Aldrich). The remaining three clones (RP11–625H13, RP11–876B4, and RP11–28L10) located in the 3′ region were labelled with Spectrum-Orange.

Samples with available FFPE-whole slides or included in tissue microarrays (TMA) were used for this analysis (Supplementary Table 2). FFPE sections were mounted on positively charged slides (SuperFrost, Thermo Scientific) following the Histology FISH Accessory Kit (DAKO) instructions as previously described [23]. Tissue sections were deparaffinized in xylene, rehydrated through a series of ethanol solutions, and treated with 2-[N-morpholino] ethanesulphonic acid (MES) and pepsin for protein digestion. Then, samples were denatured in the presence of the FISH probe and allowed to hybridize overnight in a humid chamber. Subsequently, the slides were washed and mounted with DAPI (Sigma Aldrich).

Two independent investigators (MCM and SR-P) manually scored the FISH signals by examining the number of nuclei with split signals, assessing presence of *MAML3*-fusions.

PD-L1 quantification by immunohistochemistry (IHC)

PD-L1 IHC was performed and evaluated as described in Calsina et al. [10]. Samples with available FFPE-whole slides or included in TMA were used for this analysis (Supplementary Table 2).

MAML3-fusion validation techniques

The *MAML3*-tumor candidates were validated using either PCR or an RNA fusion NGS panel.

PCR

Total RNA from candidate tumours was reverse-transcribed and used for PCR amplification with specific primers adjacent to upstream and downstream regions of the previously reported fusions [3,13]: upstream *UBTF* (exon 17: 5′-GGAGCAGCAAAAGCAGTACA-3′ and exon 19: 5′-CCCAAACCCCCCAAATC CAG-3′) and downstream *MAML3* of the fusion transcript (5′ TCTCCATTAAGTGGTGGTGGATCGAG 3′). Fusion amplicons underwent sanger sequencing.

RNA fusion NGS panel

A customized Archer's FusionPlex panel (FusionPlex *MAML3* Supplement 22729 concatenated with FusionPlex Lung v2 18090 v1.3 v1.0, Archer®) was used. The design incorporated a spike-in panel consisting of primers that covered the five *MAML3* gene exons, both in 5′ and 3′ directions.

Library preparation used 300 ng of RNA input per sample with the Archer Universal RNA reagent Kit v2 and Archer Molecular Barcode (MBC) Adapters for Illumina, following the manufacturer's instructions. Libraries were quantified using the KAPA Library Quantification Kit (Roche), and pooled equimolarly.

Sequencing was performed on the MiSeq™ System from Illumina, ensuring at least 1 million paired-end reads with 150 bp read length. The generated sequencing data were analysed using Archer Analysis v7 software developed by ArcherDX. Samples were deemed positive if the fusion breakpoint had at least three unique start site reads.

Additional OMIC-analyses on the Set 2 transcription matrix

RNA-Seq analyses and TME profiling

The data used for candidate identification through gene expression signature included microarrays (COMETE-derived, Evenepoel and CNIO microarrays) and RNA-Seq (CNIO series 1, 2 and TCGA) data. Due to the challenge of integrating data from both technologies for whole-transcriptomic analyses, microarray datasets were excluded from further analyses. Thus, we proceeded only with RNA-Seq data (CNIO series 1,2 and TCGA), comprising 349 samples and referred to as "Set 2″ hereafter. This set included a balanced number of non-metastatic and metastatic patient samples, employed for subsequent differential expression analysis (DE) using DESeq2 [24], gene set enrichment analysis (GSEA) and immune cell-type estimation. The study workflow is summarized in Supplementary Figure 1.

Gene set enrichment analysis (GSEA)

GSEA was performed using software version 2.2.2. (RRID:SCR_003199), focusing on the Molecular Signature Database (MSigDB) collections, specifically the 'H: hallmark gene sets'. Analysis was conducted using default settings, comparing *MAML3*-tumours against other genotypes using the Set 2 RNA-Seq matrix data.

Immune cell type estimation

The absolute abundance of 22 immune cell subtypes in each sample from Set 2 was estimated with CIBERSORTx [25] using the DESeq2 normalized expression matrix. Analysis parameters were as follows: (1) Gene signature matrix: LM22, containing gene expression profiles of 22 immune cell subsets; (2) 1000 permutations to obtain robust and reliable results; (3) B-mode batch correction to account for any potential batch effects, and (4) Quantile normalization disabled.

Immunohistochemistry and image data quantification

IHC analysis of CD31, CD8, CD68, CD163 and perforin was conducted on a subset of available FFPE samples. Sections (2–3 μm) were prepared and dried overnight at 60 °C. Staining was performed using the BOND-MAX Automated IHC system from Leica Microsystems GmbH and AS-Link 48 from DAKO, following standard protocols.

Sections were initially deparaffinised and pretreated with Epitope Retrieval Solution 2 (EDTA buffer pH 8.8) at 98 °C for 20 min. After washing, peroxidase blocking was conducted for 10 min using the Bond Polymer Refine Detection Kit DC9800 from Leica Microsystems GmbH.

Tissues were washed and incubated with the appropriate primary antibodies: mouse anti-CD31 (Ready to Use (RTU), mouse monoclonal [JC70A], Dako (IR610/IS610)), mouse anti-CD8 FLEX (RTU, mouse monoclonal [C8/144B], Dako (IR623), visualization system: EnVision FLEX + Mouse + Magenta), mouse anti-CD68 (RTU, mouse monoclonal [KP1]), mouse anti-CD163 (dilution: 1:200, mouse monoclonal [10D6], Leica (NCL-CD163)), and mouse anti-perforin (dilution: 1:50, Mouse Monoclonal [5B10], Abcam (ab89821). Dual IHC staining for CD8 and perforin was conducted. Cells positive for both CD8 and perforin were categorized as cytotoxic T lymphocytes (CTLs), whereas cells positive for perforin alone were classified as natural killer (NK) cells.

Tissues were incubated with anti-mouse or anti-rabbit secondary antibody with polymer or envision flex for 10 min and developed with DAB or magenta chromogen for 10 min. The slides were then stained with haematoxylin, dehydrated, cleared, and mounted with a permanent mounting medium for microscopic evaluation. Whole slide images were scanned using the AxioScan Z1 from Zeiss and captured

with either Zen Blue software (ZEN Digital Imaging for Light Microscopy, Zeiss, RRID:SCR_013672) or AxioVision software (AxioVision Imaging System, RRID:SCR_002677).

Vascular patterns (CD31) in whole tissue sections were examined by a pathologist (E. C.). Blood vessels were analysed using a workflow combining QuPath [26] and Fiji (Image J). Five regions of interest (ROIs) were chosen per tumour for vessel detection using QuPath. Images from each ROI were skeletonized in Fiji with default settings. Skeletonization data were processed using GraphPad Prism 9 and Microsoft Excel obtaining vessel length, number and branching data, subsequently combined to classify the seven vascular phenotypes described in the article.

CD8 + , CD68 + , and CD163 + cell counts were analysed using a digital image workflow in QuPath. The analysis focused on the same 2.5×107 μm2 ROI of each slide stained with each antibody. The pipeline automatically detected and quantified positive cells for each antibody among tumour infiltrating cells, excluding regions with immune nodules and immune cells near or within blood vessels.

Quantification, statistical analysis and sample clustering

Statistical analyses were conducted using different software packages: GraphPad Prism 9, R version 3.2.2., and IBM SPSS Statistics v19.

Categories for *p*-values are the following: *p*-value < 0.001: denoted as * ** , *p*-value between 0.001 and 0.01, denoted as * * and *p*-value between 0.01 and 0.05, denoted as * . Type of test performed, and *p*-values are given for each experiment.

Time-to-progression curves (from Set 1) were plotted based on the interval between primary tumour diagnosis and metastasis and/or recurrence onset. The risk of early metastasis or aggressive disease was assessed using a univariate logistic regression model.

Morpheus software, available at https://software.broadinstitute.org/morpheus, was used for graphical visualization, classification, and sample clustering.

Results

Transcription and methylation signatures, FISH and PD-L1 IHC are accurate screening tools to detect MAML3-fusion candidates

Unsupervised hierarchical clustering on Series 1 omics data, grouped together a total of twelve wild type (WT) cases with previously reported *MAML3*-fusion tumours [3,10,13]. Therefore, they were considered as *MAML3*-fusion candidates (Fig. 1a and b).

Four additional candidates were identified by FISH in available TMAs, and one more by positive PD-L1 IHC staining, characteristic of *MAML3*-tumours [10]. Consequently, based on omic analysis, FISH, and IHC, we identified 17 *MAML3*-fusion candidates (Fig. 1c and Supplementary Table 3).

We validated *MAML3*-fusion by RNA Fusion NGS Panel and/or PCR in 11 of these tumours. No remaining tumour tissue was available for PCR/NGS validation on candidates #1, #16 and #17 from CNIO. However, #1 and #16 were considered as positive based on FISH results. #19, #34, #35 remained as candidates since they belong to publicly available series, and we do not have access to them for validation. The fusions involved either exons 15, 17 or 19 of *UBTF* (ENST00000436088.6; NM_014233), or exon 15 of *TCF4* (ENST00000354452.8; NM_001083962.2) as the 5′ partner, and exon 2 of *MAML3* (ENST00000509479.6; NM_018717.5) as the 3´partner. Fig. 1c and Supplementary Table 3 summarize details on the 35 *MAML3*-related/potentially-related patients, including the poor-prognosis related secondary events in *ATRX* and *TERT* related aberrations: C228T (c.–124 C > T) mutation, *TERT* expression, promoter hypermethylation, and copy number gains.

Considering only the 31 validated cases, the overall prevalence of the fusion was 3.65% (n = 31/850) (Fig. 1c) and clinical data revealed 48% of the cases had aggressive or metastatic disease (n = 15/31). Excluding non-metastatic patients with less than 2 years of follow-up (n = 8) increased this percentage to 65% (n = 15/23), which is comparable to the percentage of metastatic cases in *SDHB*-carriers [8]. Most patients had single PCC (29/31, 93%) with a predominantly noradrenergic phenotype (27/31, 87%). Sex distribution was 58% male and 42% female, with a mean diagnosis age of 53 years (Fig. 1c and Supplementary Table 3).

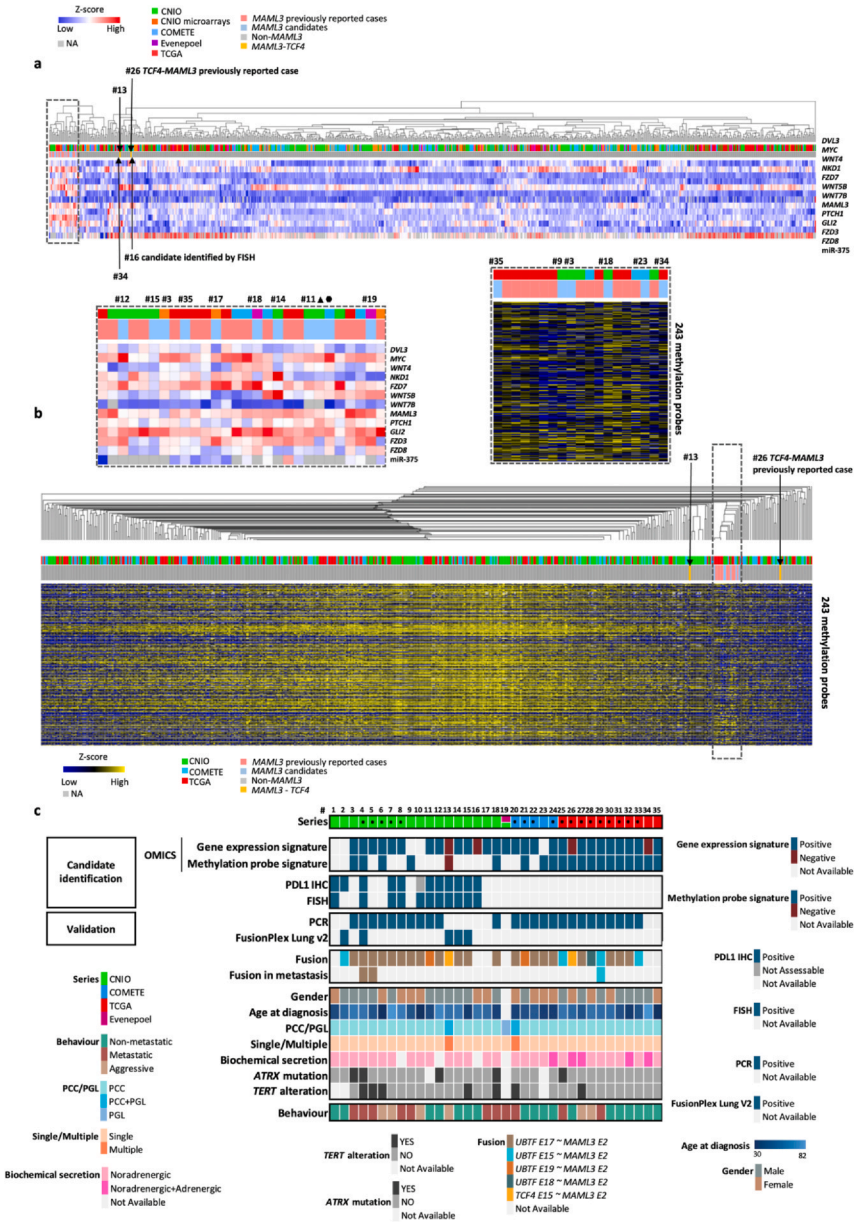

Fig. 1. *MAML3* screening on Set 1. a Unsupervised hierarchical clustering of transcriptomic *MAML3*-fusion associated profile (Average Euclidean distance). Previously reported *MAML3*-fusion cases from their respective series coloured in red, new *MAML3*-candidates in blue and *MAML3*-*TCF4* fusion cases in yellow. **b** Unsupervised hierarchical clustering of methylation profiles (Jaccard distance). Previously reported *MAML3*-fusion cases from their respective series coloured in red, new *MAML3*-candidates in blue and *MAML3*-*TCF4* fusion cases in yellow. **c** *MAML3*-related/potentially-related patients overview: clinical and molecular characteristics. Figure based on results from primary tumours. Black dots in the series represent previously reported cases. Fusion study was performed in available metastases.

Somatic post-zygotic MAML3-fusions cause multiple tumours

Candidate #13, identified by FISH, did not group with *UBTF-MAML3* tumours (Fig. 1a and b). Subsequently, NGS fusion detection panel uncovered a *TCF4* E15-*MAML3* E2 fusion, explaining the distinct omic profile. This patient presented with a PCC and multiple PGLs. The NGS fusion detection panel identified the same fusion in two PGLs, but not in the blood. Additionally, both FFPE tumours showed positive PD-L1 IHC.

In the COMETE-derived series, patient #20 with a PCC and two PGLs clustered with the *MAML3* group. Both PGLs exhibited the *UBTF* E17-*MAML3* E2 fusion, but the PCC and blood could not be tested. Interestingly, one PGL had a secondary *ATRX*-PV, and the other had *TERT* alteration (Fig. 1c). These findings in two patients with multiple PPGLs suggest a somatic post-zygotic *MAML3*-fusion event.

Impact of ATRX-PV and TERT alterations on risk of metastases in MAML3-tumours

Univariate logistic regression showed that *MAML3*-fusions significantly increases metastatic risk (OR [95% CI]: 4.696 [2.158–11.443], p = 1.654 E-04), similar to *SDHB*-tumours (OR [95% CI]: 11.440 [6.161–21.240], p = 1.717 E-14). Additionally, *MAML3*-tumours had a shorter time to progression (p = 1.712

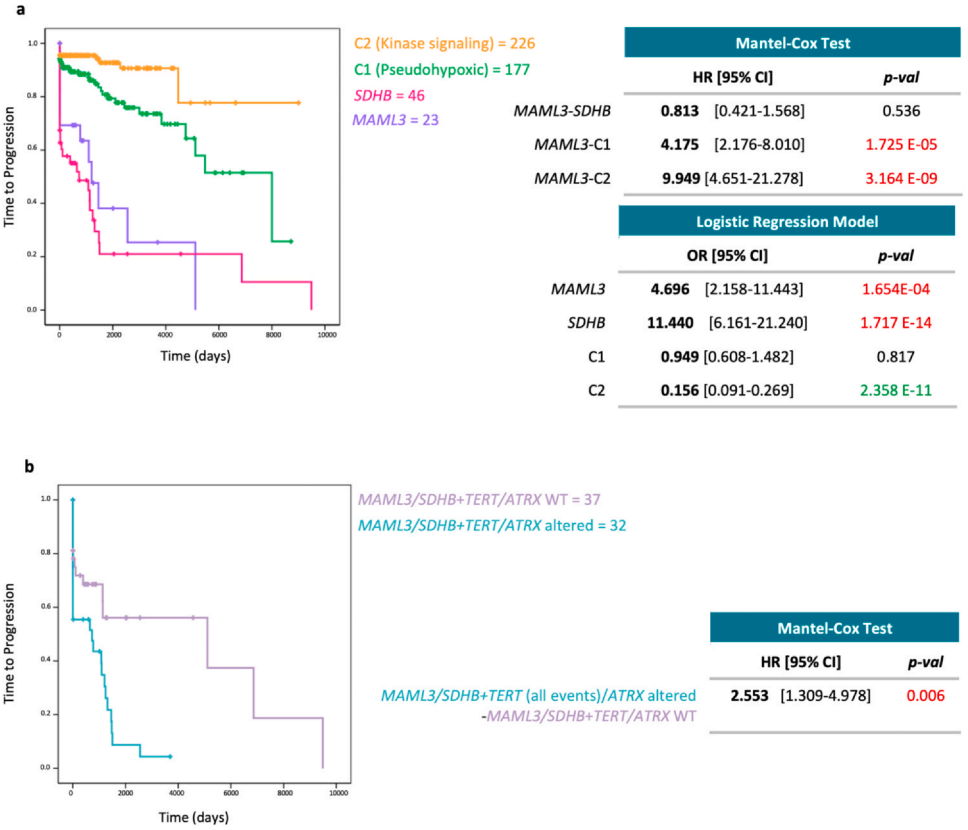

Fig. 2. Set 1 Time to Progression Curves. a Kaplan–Meier plot of time to progression according to cluster and genotype. C1 included all pseudohypoxic tumours except *SDHBs*. Each group is indicated in a different colour (time to progression: time elapsed between the diagnosis of the first PPGL and the first documented metastasis/aggressive signs). Log rank < 0.0001. **b** *MAML3*+*SDHB* samples grouped according to *ATRX*-PV and *TERT* events (*TERT* promoter mutations, *TERT* promoter hypermethylation, copy number alteration in 5p and *TERT* overexpression). Patients without metastases were censored at the date of the last follow-up. Log rank < 0.01. Mantel-Cox and Logistic Regression are shown in respective tables.

E-24) compared to C1 and C2 clusters (Fig. 2a). Due the fact that both *SDHB* and *MAML3* show a much higher risk of metastasis than other genotypes, we grouped them together for further analysis on the effect of *TERT* and *ATRX* alterations on this risk, given their association with PPGL aggressiveness [12,13]. We evaluated their prognostic value and found that *MAML3*/*SDHB*-cases with these secondary alterations presented a shorter time to progression compared to the ones without them (HR[95% CI]: 2.553 [1.309–4.978], p = 0.006) (Fig. 2b).

Impact of MAML3-fusion on MYC-targets, angiogenesis, and Ne-MT processes

We performed DE and GSEA analysis comparing *MAML3*-tumours vs other genotypes. A significant positive normalized enrichment score (NES > 1.22; FDR < 0.2) was obtained for three main processes: MYC-targets, Epithelial to Mesenchymal Transition (EMT), and Angiogenesis (Fig. 3a).

The upregulation of MYC-targets has been studied in several types of tumours, displaying an association with decreased survival and disease progression [27], along with alterations in the TME [28].

Exploring genes implicated in Ne-MT process, we observed that *MAML3*-tumours highly expressed mesenchymal genes such as *SNAI2* (versus C1 adj. p: 5.316 E^{-05}; C2 adj. p: 4.351 E^{-09}; *SDHB* adj. p: 9.761 E^{-07}) and *CDH2* (C1 adj. p: 0.001; SDHB adj. p: 4.890 E^{-08}), while neuroendocrine markers like *ENO2* (C1 adj. p: 0.016; C2 adj. p: 1.34 E^{-04}; SDHB adj. p: 1.49 E^{-05}) and *INSM1* (C1 adj. p: 0.09; C2 adj. p: 0.07) showed lower expression (Fig. 3b). This mesenchymal phenotype suggests dedifferentiation and reinforces their aggressiveness.

Similar to *VHL*- and *SDHB*-tumours, overexpression of *VEGF*, *EPAS1*, and *HK2* genes in *MAML3*-tumours has been described [29]. Following the identification of *Angiogenesis* as an enriched gene set in the GSEA analysis, our RNA-Seq data also showed significantly higher expression levels of these genes in *MAML3*-compared to C2- and *CSDE1*-tumours (*p*-value < 0.001) (Supplementary Figure 4a).

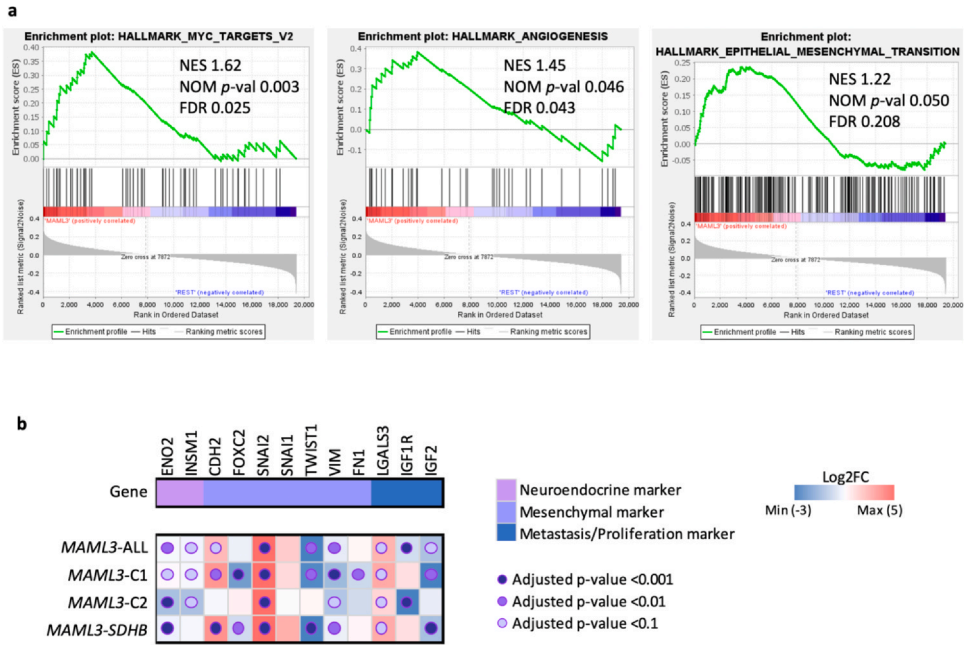

Fig. 3. Depiction of Cancer Hallmarks gene sets Enriched in *MAML3*-tumours from Set 2. a GSEA of the Cancer Hallmarks shows enriched pathways in *MAML3*-tumours compared to the rest of PPGLs with known driver gene. **b** Differential expression of Ne-MT genes and proliferation markers. Results obtained from DE analysis comparing *MAML3*-tumours vs ALL (C1 +C2 +*CSDE1*), C1, C2 and *SDHB*-tumours.

Additional analyses pointed to more differences between *MAML3*- and *CSDE1*–tumours. GSEA revealed significant positive NES (NES > 1.64; *p*-val < 0.0001) in several cancer hallmarks gene sets (Supplementary Figure 3), highlighting differences in vascular processes and immune infiltration within cluster C3 counterparts. This suggests that *MAML3* and *CSDE1* tumours do not belong to the same transcriptional cluster as has been described before.

MAML3-tumours show unique vascular architecture

CD31 IHC analysis revealed a heterogeneous vascular pattern in *MAML3*- and in metastatic tumours from other genotypes, but a homogeneous pattern in non-metastatic cases. *MAML3*-tumours had the highest number of vessels and a greater proportion of long vessels compared to *VHL*-tumours and other PPGLs (Fig. 4a and Supplementary Figure 6). For vessel branching, the highest values were detected in *MAML3*-, *VHL*- and metastatic *SDHB*-tumours.

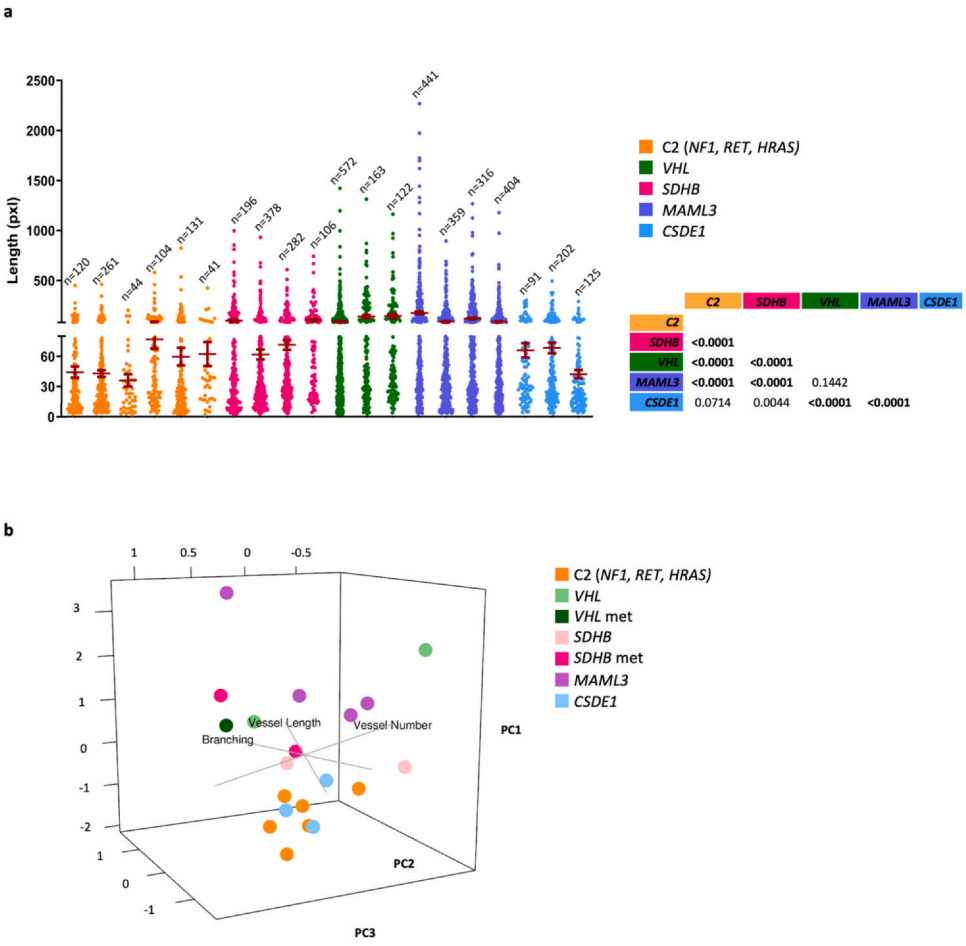

Fig. 4. Vascular Landscape of PPGLs. a Vessel length measurements per vessel. The number of vessels detected by QuPath is shown. Each column represents one tumour from one patient. Genotypes are represented by a colour. *p*-values from unpaired t-test comparing medians from each group are displayed. **b** PCA based on vessel length, number of branches per vessel and total number of vessels. *MAML3*-, *VHL*- and metastatic *SDHB*-tumours group together; as well as *CSDE1*- and C2-tumours. ***met***: metastatic case.

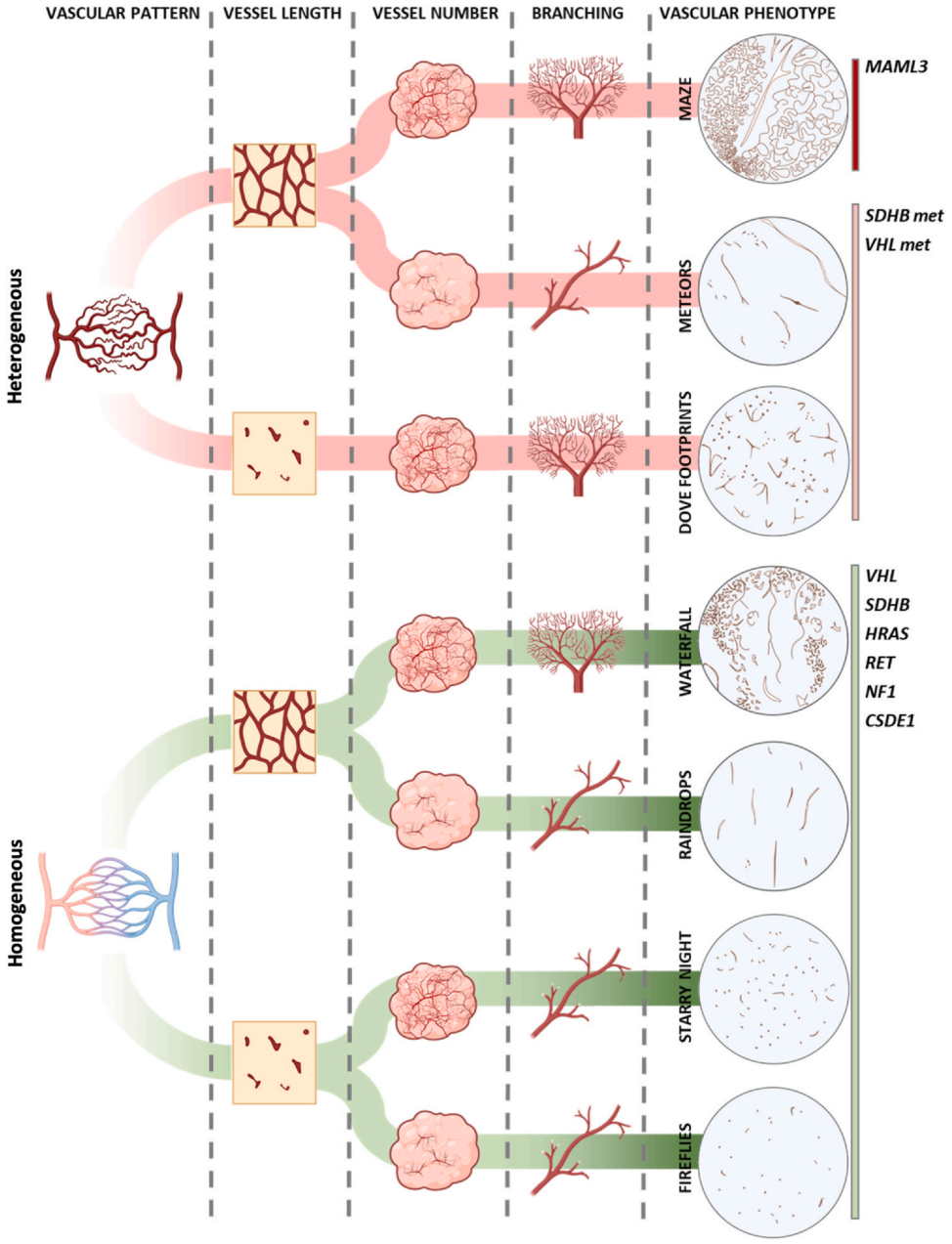

Fig. 5. Schematic Vasculature Profile. Schematic representation of the vascular phenotypes based on skeletonization data. Classification levels: (1) *Vascular pattern*: pattern of homogeneity/heterogeneity from whole tissue section based on pathologist evaluation, (2) *Vessel length*: length of the detected vessels, (3) *Vessel number*: number of vessels counted, and (4) *Branching*: number of total branches in the detected vessels. *Vascular phenotype*: classification of tumours according to 7 observed phenotypes: Maze, Meteors, Dove Footprints, Waterfall, Raindrops, Starry Night and Fireflies. Genotypes in each vascular phenotype are presented. ***met***: metastatic case. Figure created with BioRender.com.

Principal component analysis (PCA) based on these 3 features clustered *MAML3*-, *VHL*- and metastatic *SDHB*-tumours together, while C2- and *CSDE1*-tumours formed a separate group (Fig. 4b). Based on this, we created a classification system comprising 7 vascular phenotypes (Fig. 5).

The 'Maze' phenotype, exclusive to *MAML3*-tumours, featured a highly heterogeneous vascular pattern with extensive, numerous and richly branched vessels, forming long arches and networks (Fig. 5, Supplementary Figures 6 and 7).

The 'Meteors' and 'Dove footprints' phenotypes resembled *MAML3*-tumours but with less aggressive-related vascular features (Fig. 5 and Supplementary Figures 6 and 7), while 'Waterfall', 'Raindrops', 'Starry night' and 'Fireflies' displayed homogeneous patterns with few, short, and low branched vessels (Fig. 5 and Supplementary Figure 6 and 7).

Given the vascular pattern of *MAML3*-tumours, we aimed to study the extracellular matrix (ECM) features and identified a signature of 90 significant (adj. p-value < 0.05) ECM-related genes from a previously described list of 328 [30], the dysregulation of which likely impacts vascular architecture and metastatic potential (Supplementary Figure 5).

Immune infiltration in MAML3-tumours

DE analysis of *MAML3*-tumours compared to C1-, C2-, and *SDHB*-tumours identified higher expression of several immunoregulators [31] like *CD274* (PD-L1), *CD40*, *IL1A*, *IL1B* and *PRF1* (perforin) (adj. p-value < 0.1), with lower expression of MHC antigen-presenting molecules like HLA-DQB2 (Fig. 6a). With the aim to explore the immune infiltration of these tumours, we used the CIBERSORT output, unveiling a significantly higher abundance of NK-resting cells and a lower number of activated dendritic cells (DC) in *MAML3*- compared to other groups (Fig. 6b; Supplementary Figure 8). CD8 and perforin IHC staining confirmed increased CD8 + lymphocyte infiltration in *MAML3*-tumours [10], and revealed NK cell presence in PPGL for the first time (Fig. 7a and d). Finally, CD68 and CD163 IHC staining, showed higher M2

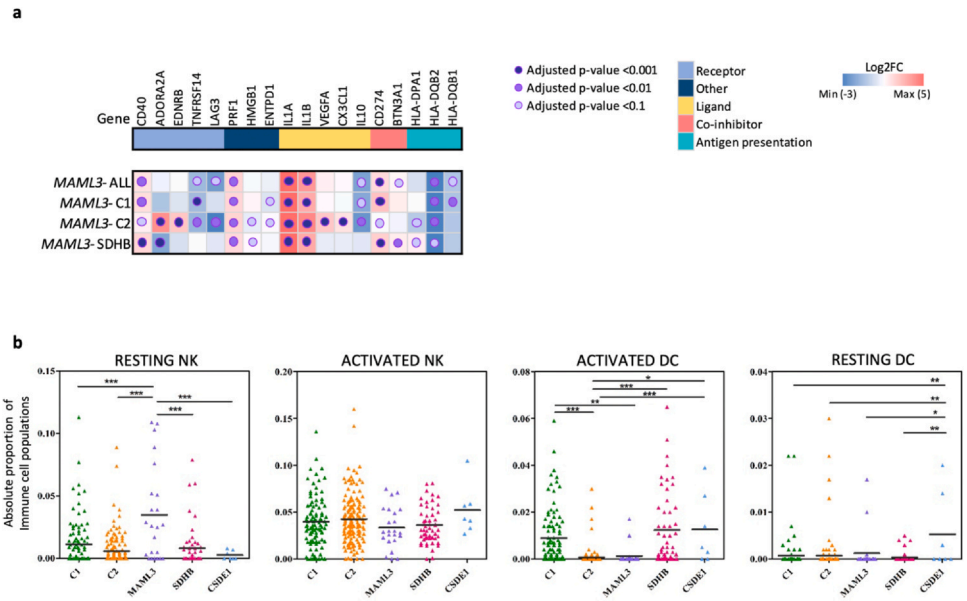

Fig. 6. Immune Infiltration Overview. a DE of significant immune markers (Thorsson et al., 2018), obtained from comparisons between *MAML3*-tumours vs ALL samples (C1 +C2 +*CSDE1*), C1 samples, C2 samples and *SDHB*-tumours. **b** Detailed representation of immune populations showing statistically significant differences when comparing *MAML3*-tumours versus C1 (excluding *SDHB*-tumours), C2, *SDHB*- and *CSDE1*-tumours.

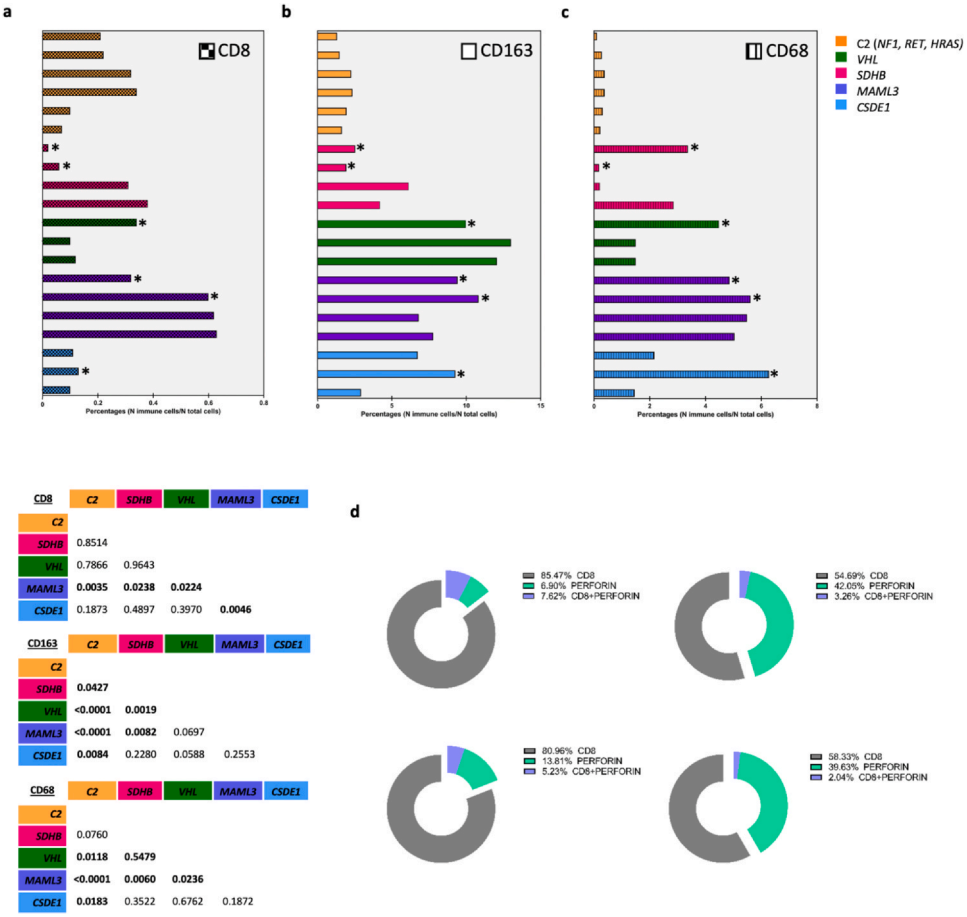

CD8	C2	SDHB	VHL	MAML3	CSDE1
C2					
SDHB	0.8514				
VHL	0.7866	0.9643			
MAML3	**0.0035**	**0.0238**	**0.0224**		
CSDE1	0.1873	0.4897	0.3970	**0.0046**	

CD163	C2	SDHB	VHL	MAML3	CSDE1
C2					
SDHB	**0.0427**				
VHL	**<0.0001**	**0.0019**			
MAML3	**<0.0001**	**0.0082**	0.0697		
CSDE1	**0.0084**	0.2280	0.0588	0.2553	

CD68	C2	SDHB	VHL	MAML3	CSDE1
C2					
SDHB	0.0760				
VHL	**0.0118**	**0.5479**			
MAML3	**<0.0001**	**0.0060**	**0.0236**		
CSDE1	**0.0183**	0.3522	0.6762	0.1872	

Fig. 7. Detailed Immune Infiltration of *MAML3*-tumours. a Percentage of CD8 + cell count per total number of cells. **b** Percentage of CD163 + cell count per total number of cells. **c** Percentage of CD68 + cell count per total number of cells. Each genotype is represented by a colour. *p*-values from unpaired t-test comparing medians from each group are displayed. Each column represents one tumour from one patient. Metastatic and aggressive cases are indicated with "* ". **d** Analysis of CD8 + lymphocyte and NK population in available *MAML3*-tumours: percentage of CD8 + lymphocytes (CD8 staining, in grey), CTLs (CD8 and perforin staining, in purple) and NK cells (perforin staining, in green) over the total number of positively stained cells. Each circle represents one tumour from one patient.

macrophages abundance in *MAML3*- and other metastatic tumours from different genotypes (Figs. 7b and 7c, Supplementary Figure 9), in agreement with previous reports [10].

Discussion

This study characterizes *MAML3*-positive PPGLs, revealing their unique TME and demonstrating that *MAML3*-fusions are somatic events often found in single noradrenergic PCCs with higher metastatic potential compared to other genotypes [32,33].

The presence of the same fusion in multiple tumours within the same patient suggests post-zygotic somatic mosaicism. While post-zygotic events have been described in *EPAS1*- and *H3–3A*-tumours [34,35], *MAML3*-fusions have not been associated with such events. Therefore, although most *MAML3*-positive patients have a single noradrenergic PCC, WT-patients with multiple tumours could also be fusion-candidates, though this occurrence is very rare (7% of *MAML3*-cases and 0.25% of all PPGLs).

SDHB-loss has been previously associated with poor prognosis [36]. Herein we demonstrate that *MAML3*-fusions exhibit a similar behaviour; therefore, *MAML3*-tumour patients could be clinically managed in a similar manner. Both genotypes show shorter time to progression compared to C1- and C2-tumours, consistent with TCGA data [3]. When *TERT* and *ATRX* events are considered, the time to progression decreases significantly, suggesting these secondary events are key factors determining higher metastatic risk [12,13]. Somatic *ATRX*-PVs are mainly found in fusion-positive tumours, potentially linked to higher instability, neoantigen load, and tumour mutational burden in *MAML3*-tumours [10]. *TERT* events are more frequent in *SDHB*-related tumours [10,13]. Further research is needed to understand the accumulation of poor prognostic secondary events in these two genotypes.

MAML3-fusion-Induced Wnt and MYC pathways dysregulation may promote tumour aggressiveness

MAML3-driven tumours activate the Wnt/β-catenin pathway [3], and stable β-catenin relocates to the nucleus, where its binds transcription factors activating target genes, such as *MYC* [37]. In our series, *MAML3*-tumours overexpress *MYC* and activate MYC-targets. UBTF and TCF4 are MYC-targets [38–42], and also bind β-catenin. That would establish a positive feedback loop on the Wnt-pathway, which is associated with cell progression, growth, and enhanced viability [11]. This metastatic potential could be additionally explained by the increased expression of mesenchymal markers like *SNAI2* [43–46]. Interestingly, several drugs targeting Wnt-signaling pathway are being tested in clinical trials [47].

MAML3-tumours: unique vascular and ECM characteristics

Heterogeneous vascular patterns in PPGLs have been linked to higher metastatic risk, while homogeneous patterns are seen in non-metastatic PPGLs [48]. Our study finds that *MAML3*-tumours exhibit these metastatic-associated vascular patterns. Detailed vessel analysis classifies *MAML3*-tumours into a distinct group, significantly different from other genotypes, including *CSDE1*-PPGLs.

The composition of the ECM plays a pivotal role in angiogenesis [49,50]. Herein, we show that *MAML3*- tumours exhibit a distinct ECM profile, characterized by *VEGF* overexpression that could lead to the formation of new blood vessels [3,11,51]. Moreover, they present a transcriptional profile between C1 and C2, distinct from *CSDE1*-tumours [29], with pseudohypoxic features such as *EPAS1* overexpression, linked to tumour migration and invasion [52].

Unique immune characteristics of MAML3-tumours open the window to potential new therapeutic strategies

The clonal development of malignant cells relies on a specific tissue environment referred to as the TME, which aggregates cellular and noncellular components, such as immune cells and the ECM [53]. Although PPGL are considered "immunologically cold" tumours [54], those related to *MAML3*-fusions present a major CD8 + lymphocytes and M2 macrophages abundance, together with a higher PD-L1 expression compared to other genotypes [10].

In addition, our findings reveal the presence of NK-resting cells, which represent a potential target treatment [55,56]. DCs interactions with NK and CD8 + lymphocytes are fundamental in TME modulation and promotion of anti-tumour responses [57]. Mature tumour-infiltrating DC enhance NK activity through IL12 secretion [58]. Although *MAML3*-tumours present infiltrated NK cells, their inactivity is possibly related to the presence of catecholamines [59] and a lower DC abundance, which could be also influenced by elevated levels of *VEGF* [60].

Our study identifies not only elevated PD-L1 levels, but also CD40 overexpression in these samples, reinforcing the need to develop patient-specific immunotherapies. CD40 agonists have been used to enhance antitumour immunity [61]. These agents have shown efficacy in PPGL mouse models [62] and in clinics, particularly when used together with anti-VEGF [63,64]. Considering the *VEGF* overexpression and rich vasculature observed in *MAML3*-tumours, this combination emerges as a promising therapeutic option for these patients.

Given that CD8+ activation [65] and NK regulation impact anti-PD1/PD-L1 response [66], activation of the NK-DC axis arises as a potential therapeutic strategy to increase anti-PD1/PD-L1 sensitivity in *MAML3*-tumours. In this respect, it is important to note that anti-PD1/PD-L1 therapy has already been

tested in mPPGLs, with limited efficacy [67]. However, *MAML3* genotype status was unknown in this study, and it is tempting to speculate that these patients might benefit from immunotherapy.

Globally, our work aimed to establish the *MAML3* fusion prevalence on an outstanding series, characterize the associated phenotype, and uncover vulnerabilities. The 3.65% prevalence of *MAML3*-fusion in this series may be underestimated, as only *UBTF-MAML3* tumours and not *TCF4-MAML3*, showed consistent clustering in omic data. For *MAML3*-fusion screening within the genetic diagnosis framework, we recommend testing clinically suspicious WT patients (single PCC, noradrenergic secretion) without familial history. In candidates, PD-L1 IHC staining should be performed, followed by fusion validation through FISH, NGS or PCR. With their distinctive microenvironment marked by a rich vasculature and unique immune profile, *MAML3*-tumours present new opportunities for targeted and combination therapies.

Research agenda

- Further investigation into the use of CD40 agonists and anti-VEGF for *MAML3*-related PPGLs treatment is necessary.
- Evaluating *MAML3* genotype in previous trials with limited anti-PD1/PD-L1 response could reveal potential benefits of immunotherapy for these patients.
- Targeting NK-DC axis activation in *MAML3*-tumors could be a promising strategy to improve anti-PD1/PD-L1 therapy effectiveness.

Practice points

- Up to 70% of PPGL patients carry germline or somatic pathogenic variants in known disease-causing genes.
- Genetic profiling of PPGLs is currently part of the routine clinical practice and guides patient management and follow-up.
- Around 20% of the patients present with metastatic disease and current treatments show limited efficacy, besides their molecular and biochemical differences.
- *MAML3*-fusion related PPGLs show a distinct transcriptional and methylation profile and are associated with an aggressive tumour behaviour.
- *MAML3*-fusions occur in 4% of tumours and tend to accumulate secondary events.
- PD-L1 overexpression is a characteristic of *MAML3* tumours.
- *MAML3*-tumours show elevated expression of neuroendocrine-to-mesenchymal transition markers, MYC-target genes, and angiogenesis-related genes.
- *MAML3*-tumours present a distinctive microenvironment, marked by a rich vasculature and unique immune profile, which present new opportunities for targeted and combined therapies.

Funding

This work was supported by Project PI17/01796 and PI20/01169 to M.R. [Instituto de Salud Carlos III (ISCIII), Acción Estratégica en Salud, cofinanciado a través del Fondo Europeo de Desarrollo Regional (FEDER)], Paradifference Foundation [no grant number applicable to M.R.], Pheipas Association [no grant number applicable to M.R.], Spanish National Research and Development Plan, Instituto de Salud Carlos III, and FEDER (PI20/01837 to S.R-P), and Asociación Española Contra el Cancer (AECC-LABAE20049RODR to S.R-P.). M.E.S.H is supported by ISCIII (Project: IMPaCT_VUSCan, Ref. PMP22/00064) A.M.M.M. was supported by CAM (S2017/BMD-3724; and Paradifference Foundation), M.M. and S.M. are supported by

the Spanish Ministry of Science, Innovation and Universities "Formación del Profesorado Universitario—FPU" fellowship with ID number FPU18/00064, and FPU19/04940. E.A. is supported by CAM (P2022/BMD-7379, iTIRONET-CM). C.R. is supported by the CNIO Friends Postdoctoral Contract Program. A.D.T. is supported by the Centro de Investigacion Biomédica en Red de Enfermedades Raras (CIBERER). L.J.L.G. was supported by La Caixa Postdoctoral Junior Leader Fellowship (LCF/BQ/PI20/11760011). A.F.S. received the support of a fellowship from La Caixa Foundation (ID 100010434; LCF/BQ/DR21/11880009). C.M.C. was supported by a grant from the AECC Foundation (AIO15152858 MONT). F.B. and S.N. were supported as part of an Immuno-TargET project under the umbrella of University Medicine Zurich. N.B. and G.E. were financially supported by the Deutsche Forschungsgemeinschaft (DFG, German Research Foundation) within the CRC/Transregio 205/1, Project No. 314061271 - TRR205 "The Adrenal: Central Relay in Health and Disease".

CRediT authorship contribution statement

María Monteagudo: Conceptualization, Methodology, Formal analysis, Investigation, Data curation, Writing – original draft, Writing – review & editing, Visualization, Supervision. **Bruna Calsina:** Conceptualization, Methodology, Investigation, Data curation, Writing – review & editing, Supervision. **Milton E. Salazar-Hidalgo:** Conceptualization, Investigation, Writing – original draft, Writing – review & editing. **Ángel M. Martínez-Montes:** Methodology, Software, Writing – review & editing, Visualization. **Elena Piñeiro-Yáñez:** Methodology, Software. **Eduardo Caleiras:** Methodology, Software, Formal analysis, Investigation. **Maria Carmen Martín:** Investigation. **Sandra Rodríguez-Perales:** Methodology, Investigation. **Rocío Letón:** Methodology. Methodology. **Eduardo Gil:** Methodology. **Alexandre Buffet:Nelly Burnichon:** Methodology, Resources. **Ángel Fernández-Sanromán:** Methodology. **Alberto Díaz-Talavera:** Investigation. **Sara Mellid:** Investigation. **Ester Arroba:** Investigation, Writing – review & editing. **Clara Reglero:** Writing – review & editing. **Natalia Martínez-Puente:** Investigation. **Giovanna Roncador:** Methodology, Investigation. **Maria Isabel del Olmo:** Resources. Resources. **Pedro José Pinés Corrales:** Resources. **Cristina Lamas Oliveira:** Resources. **Cristina Álvarez-Escolá:** Resources. **María Calatayud Gutiérrez:** Resources. **Adrià López-Fernández:** Resources. **Nuria Palacios García:** Resources. **Rita María Regojo:** Resources. **Luis Robles Díaz:** Resources. **Nuria Romero Laorden:** Resources. **Oscar Sanz Guadarrama:** Resources. **Nicole Bechmann:** Resources. **Felix Beuschlein:** Resources. **Letizia Canu:**: Resources. **Graeme Eisenhofer** Resources. **Martin Fassnacht:** Resources. **Svenja Nölting:** Resources. **Marcus Quinkler:** Resources. **Elena Rapizzi:** Resources. **Hanna Remde:** Resources. **Henri J. Timmers:** Resources. **Anne-Paule Gimenez-Roqueplo:Cristina Rodriguez-Antona:** Writing – review & editing. **Maria Currás-Freixes:** Data curation. **Fatima Al-Shahrour:** Methodology, Software. **Alberto Cascón:** Data curation, Writing – review & editing. **Luis J. Leandro-García:** Writing – review & editing, Supervision. **Cristina Montero-Conde:** Methodology, Formal analysis, Investigation, Writing – review & editing, Supervision. **Mercedes Robledo:** Conceptualization, Methodology, Resources, Data curation, Writing – review & editing, Supervision.

Declaration of Competing Interest

Authors declare no competing interests.

Acknowledgments

We thank the Spanish National Tumour Bank Network (RD09/0076/00047) and the General Hospital of Albacete Biobank for the support in obtaining tumour samples and all patients and physicians involved in the study. We also thank the Action COST Harmonisation (CA20122) for supportive networking.

Appendix A. Supporting information

Supplementary data associated with this article can be found in the online version at doi:10.1016/j.beem.2024.101931.

References

[1] Dahia PLM. Pheochromocytomas and paragangliomas, genetically diverse and minimalist, all at once!. Cancer Cell 2017;31:159–61.
[2] Cascón A, et al. Genetic bases of pheochromocytoma and paraganglioma. J Mol Endocrinol 2023;70.
[3] Fishbein L, et al. Comprehensive molecular characterization of pheochromocytoma and paraganglioma. Cancer Cell 2017;31:181–93.
[4] Nölting S, et al. Personalized management of pheochromocytoma and paraganglioma. Endocr Rev 2022;43:199–239.
[5] Ayala-Ramirez M, et al. Clinical risk factors for malignancy and overall survival in patients with pheochromocytomas and sympathetic paragangliomas: primary tumor size and primary tumor location as prognostic indicators. J Clin Endocrinol Metab 2011;96:717–25.
[6] Fassnacht M, et al. Adrenocortical carcinomas and malignant phaeochromocytomas: ESMO-EURACAN Clinical Practice Guidelines for diagnosis, treatment and follow-up. Ann Oncol 2020;31:1476–90.
[7] Eisenhofer G, et al. Plasma methoxytyramine: a novel biomarker of metastatic pheochromocytoma and paraganglioma in relation to established risk factors of tumour size, location and SDHB mutation status. Eur J Cancer 2012;48:1739–49.
[8] Amar L, et al. Succinate dehydrogenase B gene mutations predict survival in patients with malignant pheochromocytomas or paragangliomas. J Clin Endocrinol Metab 2007;92:3822–8.
[9] Castro-Vega LJ, et al. Multi-omics analysis defines core genomic alterations in pheochromocytomas and paragangliomas. Nat Commun 2015;6.
[10] Calsina B, et al. Genomic and immune landscape Of metastatic pheochromocytoma and paraganglioma. Nat Commun 2023;14.
[11] Alzofon N, et al. Mastermind like transcriptional coactivator 3 (MAML3) drives neuroendocrine tumor progression. Mol Cancer Res 2021;19:1476–85.
[12] Monteagudo M, et al. Analysis of telomere maintenance related genes reveals NOP10 as a new metastatic-risk marker in pheochromocytoma/paraganglioma. Cancers 2021;13.
[13] Job S, et al. Telomerase activation and ATRX mutations are independent risk factors for metastatic pheochromocytoma and paraganglioma. Clin Cancer Res 2019;25:760–70.
[14] Evenepoel L, et al. Expression of contactin 4 is associated with malignant behavior in pheochromocytomas and paragangliomas. J Clin Endocrinol Metab 2018;103:46–55.
[15] Barthel FP, et al. Systematic analysis of telomere length and somatic alterations in 31 cancer types. Nat Genet 2017;49:349–57.
[16] Burnichon N, et al. Integrative genomic analysis reveals somatic mutations in pheochromocytoma and paraganglioma. Hum Mol Genet 2011;20:3974–85.
[17] López-Jiménez E, et al. Research resource: transcriptional profiling reveals different pseudohypoxic signatures in SDHB and VHL-related pheochromocytomas. Mol Endocrinol 2010;24:2382–91.
[18] Calsina B, et al. Integrative multi-omics analysis identifies a prognostic miRNA signature and a targetable miR-21-3p/TSC2/mTOR axis in metastatic pheochromocytoma/paraganglioma. Theranostics 2019;9:4946–58.
[19] De Cubas AA, et al. DNA methylation profiling in pheochromocytoma and paraganglioma reveals diagnostic and prognostic markers. Clin Cancer Res 2015;21:3020–30.
[20] Remacha L, et al. Gain-of-function mutations in DNMT3A in patients with paraganglioma. Genet Med 2018;20:1644–51.
[21] Remacha L, et al. Targeted exome sequencing of krebs cycle genes reveals candidate cancer-predisposing mutations in pheochromocytomas and paragangliomas. Clin Cancer Res 2017;23:6315–25.
[22] Remacha L, et al. Recurrent germline DLST mutations in individuals with multiple pheochromocytomas and paragangliomas. Am J Hum Genet 2019;104:651–64.
[23] Rodriguez-Perales S, et al. Truncated RUNX1 protein generated by a novel t(1;21)(p32;q22) chromosomal translocation impairs the proliferation and differentiation of human hematopoietic progenitors. Oncogene 2016;35:125–34.
[24] Love MI, Huber W, Anders S. Moderated estimation of fold change and dispersion for RNA-seq data with DESeq2. Genome Biol 2014;15.
[25] Newman AM, et al. Determining cell type abundance and expression from bulk tissues with digital cytometry. Nat Biotechnol 2019;37:773–82.
[26] Bankhead P, et al. QuPath: Open source software for digital pathology image analysis. Sci Rep 2017;7.
[27] Schulze A, Oshi M, Endo I, Takabe K. MYC targets scores are associated with cancer aggressiveness and poor survival in ER-positive primary and metastatic breast cancer. Int J Mol Sci 2020;21:1–13.
[28] Dhanasekaran R, et al. The MYC oncogene - the grand orchestrator of cancer growth and immune evasion. Nat Rev Clin Oncol 2022;19:23–36.
[29] Zethoven M, et al. Single-nuclei and bulk-tissue gene-expression analysis of pheochromocytoma and paraganglioma links disease subtypes with tumor microenvironment. Nat Commun 2022;13.
[30] Chakravarthy A, Khan L, Bensler NP, Bose P, De Carvalho DD. TGF-β-associated extracellular matrix genes link cancer-associated fibroblasts to immune evasion and immunotherapy failure. Nat Commun 2018;9.
[31] Thorsson V, et al. The immune landscape of cancer. Immunity 2018;48:812–830.e14.
[32] Jimenez C, et al. Current and future treatments for malignant pheochromocytoma and sympathetic paraganglioma. Curr Oncol Rep 2013;15:356–71.
[33] Roman-Gonzalez A, Jimenez C. Malignant pheochromocytoma-paraganglioma: pathogenesis, TNM staging, and current clinical trials. Curr Opin Endocrinol Diabetes Obes 2017;24:174–83.
[34] Zhuang Z, et al. Somatic HIF2A gain-of-function mutations in paraganglioma with polycythemia. N Engl J Med 2012;367:922–30.
[35] Toledo RA, et al. Recurrent mutations of chromatin-remodeling genes and kinase receptors in pheochromocytomas and paragangliomas. Clin Cancer Res 2016;22:2301–10.
[36] Hamidi O, et al. Outcomes of patients with metastatic phaeochromocytoma and paraganglioma: a systematic review and meta-analysis. Clin Endocrinol (Oxf) 2017;87:440–50.

[37] Reya T, Clevers H. Wnt signalling in stem cells and cancer. Nature 2005;434:843–50.
[38] Grandori C, et al. c-Myc binds to human ribosomal DNA and stimulates transcription of rRNA genes by RNA polymerase I. Nat Cell Biol 2005;7:311–8.
[39] Van Riggelen J, Yetil A, Felsher DW. MYC as a regulator of ribosome biogenesis and protein synthesis. Nat Rev Cancer 2010;10:301–9.
[40] Chen C, et al. Genome-wide ChIP-seq analysis of TCF4 binding regions in colorectal cancer cells. Int J Clin Exp Med 2014;7:4253.
[41] Forrest MP, Waite AJ, Martin-Rendon E, Blake DJ. Knockdown of human TCF4 affects multiple signaling pathways involved in cell survival, epithelial to mesenchymal transition and neuronal differentiation. PLoS One 2013;8.
[42] Delgado-Bellido D, et al. VE-Cadherin modulates β-catenin/TCF-4 to enhance vasculogenic mimicry. Cell Death Dis 2023;14.
[43] Peinado H, Portillo F, Cano A. Switching on-off snail: LOXL2 versus GSK3beta. Cell Cycle 2005;4:1749–52.
[44] Peinado H, Olmeda D, Cano A. Snail, Zeb and bHLH factors in tumour progression: an alliance against the epithelial phenotype? Nat Rev Cancer 2007;7:415–28.
[45] Moody SE, et al. The transcriptional repressor snail promotes mammary tumor recurrence. Cancer Cell 2005;8:197–209.
[46] Li J, et al. MiR-2392 suppresses metastasis and epithelial-mesenchymal transition by targeting MAML3 and WHSC1 in gastric cancer. FASEB J 2017;31:3774–86.
[47] Chen Y, Chen M, Deng K. Blocking the Wnt/β-catenin signaling pathway to treat colorectal cancer: strategies to improve current therapies (Review). Int J Oncol 2023;62.
[48] Oudijk L, et al. Vascular pattern analysis for the prediction of clinical behaviour in pheochromocytomas and paragangliomas. PLoS One 2015;10.
[49] Balcioglu HE, Van De Water B, Danen EHJ. Tumor-induced remote ECM network orientation steers angiogenesis. Sci Rep 2016;6.
[50] Kretschmer M, Rüdiger D, Zahler S. Mechanical aspects of angiogenesis. Cancers 2021;13.
[51] Greenberg JI, et al. A role for VEGF as a negative regulator of pericyte function and vessel maturation. Nature 2008;456:809–14.
[52] Holmquist-Mengelbier L, et al. Recruitment of HIF-1alpha and HIF-2alpha to common target genes is differentially regulated in neuroblastoma: HIF-2alpha promotes an aggressive phenotype. Cancer Cell 2006;10:413–23.
[53] Anderson NM, Simon MC. The tumor microenvironment. Curr Biol 2020;30:R921–5.
[54] Uher O, et al. The immune landscape of pheochromocytoma and paraganglioma: current advances and perspectives. Endocr Rev 2024;45.
[55] Verheyden S, Demanet C. NK cell receptors and their ligands in leukemia. Leukemia 2008;22:249–57.
[56] Bouwer AL, et al. NK cells are required for dendritic cell-based immunotherapy at the time of tumor challenge. J Immunol 2014;192:2514–21.
[57] Peterson EE, Barry KC. The natural killer-dendritic cell immune axis in anti-cancer immunity and immunotherapy. Front Immunol 2021;11.
[58] Zhou Y, Cheng L, Liu L, Li X. NK cells are never alone: crosstalk and communication in tumour microenvironments. Mol Cancer 2023;22.
[59] Capellino S, Claus M, Watzl C. Regulation of natural killer cell activity by glucocorticoids, serotonin, dopamine, and epinephrine. Cell Mol Immunol 2020;17:705–11.
[60] Han Z, et al. Role of hypoxia in inhibiting dendritic cells by VEGF signaling in tumor microenvironments: mechanism and application. Am J Cancer Res 2021;11:3777.
[61] Kraehenbuehl L, Weng CH, Eghbali S, Wolchok JD, Merghoub T. Enhancing immunotherapy in cancer by targeting emerging immunomodulatory pathways. Nat Rev Clin Oncol 2022;19:37–50.
[62] Caisova V, et al. The significant reduction or complete eradication of subcutaneous and metastatic lesions in a pheochromocytoma mouse model after immunotherapy using mannan-BAM, TLR ligands, and anti-CD40. Cancers 2019;11.
[63] Djureinovic D, Wang M, Kluger HM. Agonistic CD40 antibodies in cancer treatment. Cancers 2021;13:1–18.
[64] Kashyap AS, et al. Optimized antiangiogenic reprogramming of the tumor microenvironment potentiates CD40 immunotherapy. Proc Natl Acad Sci USA 2020;117:541–51.
[65] Farhood B, Najafi M, Mortezaee K. CD8+ cytotoxic T lymphocytes in cancer immunotherapy: a review. J Cell Physiol 2019;234:8509–21.
[66] Sivori S, et al. Human NK cells: surface receptors, inhibitory checkpoints, and translational applications. Cell Mol Immunol 2019;16:430.
[67] Jimenez C, et al. Phase II clinical trial of pembrolizumab in patients with progressive metastatic pheochromocytomas and paragangliomas. Cancers 2020;12:1–15.